Acta Materialia 189 (2020) 105–117

Contents lists available at ScienceDirect

Acta Materialia

journal homepage: www.elsevier.com/locate/actamat

Full length article

Kinetic processes in the high-temperature pressure-infiltration of Al into Al_2O_3

Gionata Schneider*, Marta Fornabaio, Ludger Weber, Andreas Mortensen

EPFL-STI-IMX-LMM Station 12, CH-1015 Lausanne, Switzerland

ARTICLE INFO

Article History:
Received 2 August 2019
Revised 18 February 2020
Accepted 19 February 2020
Available online 26 February 2020

Keywords:
Aluminium
Alumina
High temperature
Metal matrix composites
Wetting

ABSTRACT

We explore the influence (i) of the interaction between aluminium and alumina, and (ii) of sodium impurities present in Bayer alumina, on the pressure infiltration of alumina particle preforms with molten aluminium. At 1000°C or above, although the aluminium/alumina system is non-reactive, capillarity-driven solution-reprecipitation processes cause the liquid-solid interface to become mobile. Data show that this can result in infiltration kinetics that resemble those observed with reaction-driven pressure infiltration, namely a continuously increasing melt saturation under fixed infiltration pressure. Resulting isobaric saturation velocities are measured at 1000°C, 1050°C and 1100°C. The role of alumina particle shape and of Na-containing inclusions is investigated. It is found that the main factors affecting the rate of high-temperature isobaric infiltration in this system is the particle geometry. Measured steady infiltration rates give an activation volume on the order of $\approx 200\ nm^3$ and an activation energy in the range of 300-500 $\frac{kJ}{mol}$, suggesting that isobaric infiltration kinetics are governed by diffusion through the solid alumina. Sodium impurities of Bayer alumina are present within β''-Al_2O_3. They do not influence steady pressure infiltration but ease initial melt penetration into the preform, possibly because evaporated Na_2O alters the oxide skin layer that lines the surface of molten aluminium.

1. Introduction

Pressure infiltration, one of the main processing methods used in the production of metal matrix composites (MMCs), consists in pushing a liquid metal into a porous refractory (ceramic, carbon or metal) "preform", followed by solidification of the melt. Pressure is applied in this process to overcome capillary forces, as these usually resist penetration of the metal melt into the preform because the contact angle θ formed at the Solid-Liquid-Vapour (S-L-V) triple line is well above 0° [1–4] in most molten metal/solid ceramic systems.

Often, at the high temperatures characteristic of metallurgical processes such as infiltration, metal/preform materials interact through various kinetic phenomena that can cause θ to depend on time. If the solid and liquid phases react, a new L-S interface phase may form and gradually change the degree of wetting of the solid by the liquid. In the absence of interfacial reaction, substrate dissolution and reprecipitation may cause ridging of the L-S interface, leading again the apparent contact angle measured in a sessile drop experiment to become a function of time, similar to what is observed with reactive systems [5–9].

Time-dependent wetting is manifest in pressure infiltration by the fact that saturation (a.k.a. "drainage") curves, commonly used to characterize wetting of a given preform by a given infiltrant, cannot be measured because at fixed pressure the melt saturation no longer stabilizes. Instead, interfacial interaction between the liquid and the solid substrate lead to a steadily moving infiltration front even though the applied pressure driving the metal into the preform is kept constant. Such gradual isobaric pressure infiltration has recently been documented for a reactive system, namely a copper-silicon alloy infiltrating porous carbon [10]. In that system the interaction between the liquid and the solid leads to the formation of SiC which, being better wetted by the melt than is carbon, drives a steady advancement of the front at fixed pressure [10].

It was shown in Ref. [10] that a parallel can be drawn between the kinetics of elevated temperature pressure infiltration and the kinetics of high-temperature plasticity. Both processes involve the stress-driven, thermally activated, forward motion of a line (the L/S/V triple line or the dislocation line, respectively) past a series of fixed obstacles. Both processes have the same basic input parameters, namely temperature and applied stress, while the measured output parameter is, respectively, the rate of infiltration and the rate of plastic deformation.

In elevated temperature plasticity, the rate of deformation is often described as a thermally activated process, the activation energy of

* Corresponding author.
E-mail address: gionata.schneider@gmail.com (G. Schneider).

https://doi.org/10.1016/j.actamat.2020.02.048

which is reduced by the product of an activation volume times the applied stress. It was shown in Ref. [10] that the kinetics of reactive copper-silicon alloy infiltrating porous carbon at fixed pressure can also be described using this approach.

Here, we apply the same methodology in the analysis and interpretation of infiltration rate measurements conducted on the non-reactive Al-Al_2O_3 system at 1000°C or higher. This system has already been investigated by means of sessile drop experiments both at high (hundreds of Kelvin above the aluminium melting point) and low (slightly above the Al melting point) temperatures ([8,11–17]). The contact angle θ is known to decrease with increasing temperature, from 100° under vacuum near the Al melting point (660°C) down to roughly 70° at 1150°C.

The behaviour of this system in the context of pressure infiltration was studied by Léger *et al.* [18], who recorded saturation curves below 1000°C. At those lower temperatures, one observes a stabilization of the saturation S when the applied metal pressure P is kept constant. We show here that, at or above 1000°C, the saturation no longer stabilizes in this non-reactive system, as in the reactive Cu-46at.pct. Si/graphite system.

With the aluminium/alumina system, a further complication arises at elevated temperature, in that sodium is present as an impurity in certain nominally pure alumina powders, including those that were used in the earlier study of Léger *et al.* [18]. Sodium impurities in alumina powder are quite common due to the use of NaOH in the Bayer process [19]: this can leave residual Na atoms in the alumina, which are then generally present within inclusions of the $NaAl_{11}O_{17}$ (Na_2O $11Al_2O_3$) phase. This phase is named β''-Al_2O_3; it is a metastable [20–22] ion-conducting phase (which is used in sodium-sulphur batteries [20,21,23,24]). The equilibrium phase in the Na_2O-Al_2O_3 system is called β-Al_2O_3 and is characterized by a lower Na_2O:Al_2O_3 ratio (1:7); however, β''-Al_2O_3 transforms to β-Al_2O_3 only above 1600°C and is hence often not observed in commercial alumina particles. At the high temperatures explored here, sodium atoms might intervene in the infiltration process. We therefore address here this issue as well, notably by analysing three alumina powders that differ in particle shape or composition, to separate the role played by the presence of sodium from that played by the particle geometry.

2. Experimental

2.1. Materials

Ceramic samples were prepared using (i) an angular alumina α-Al_2O_3 F1000 (Fig. 1(e-f)) of average diameter $5\mu m$ purchased from Treibacher Schleifmittel (Laufenburg, Germany), or (ii) polygonal alumina α-Al_2O_3 AA10 particles of average diameter $10\mu m$ from Sumitomo Chemical Co., Ltd. (Osaka, Japan) (Fig. 1(a-b)). Powder X-Ray diffraction analyses reveal the presence in the F1000 powder of the Na-containing phase β''-Al_2O_3, together with α-Al_2O_3. AA10 powder X-ray diffractograms show it to be pure α-Al_2O_3.

In order to separate the effect of shape and composition of the alumina powders, a third powder was used here, namely a powder produced by reacting the pure alumina polygonal powder AA10 with sodium carbonate at 1300°C for 15h [23]. This results in the following reaction:

$$11Al_2O_3 + Na_2CO_3 \rightarrow 2NaAl_{11}O_{17} + CO_2 \quad (1)$$

which gives the AA10 powder the same sodium-containing phase as the F1000 Bayer alumina powder. Varying the reaction time and temperature, different molar ratios of Na_2O:Al_2O_3 can be produced. To reproduce as closely as possible the composition of the F1000 powder, AA10 powder was reacted to produce a ratio of 1:15 Na_2O:Al_2O_3. The so-produced powder has the same size and morphological features as the AA10 alumina powder, but a composition close to that of the F1000 alumina powder. It is hereafter named β''-AA10 (Fig. 1(c-d)).

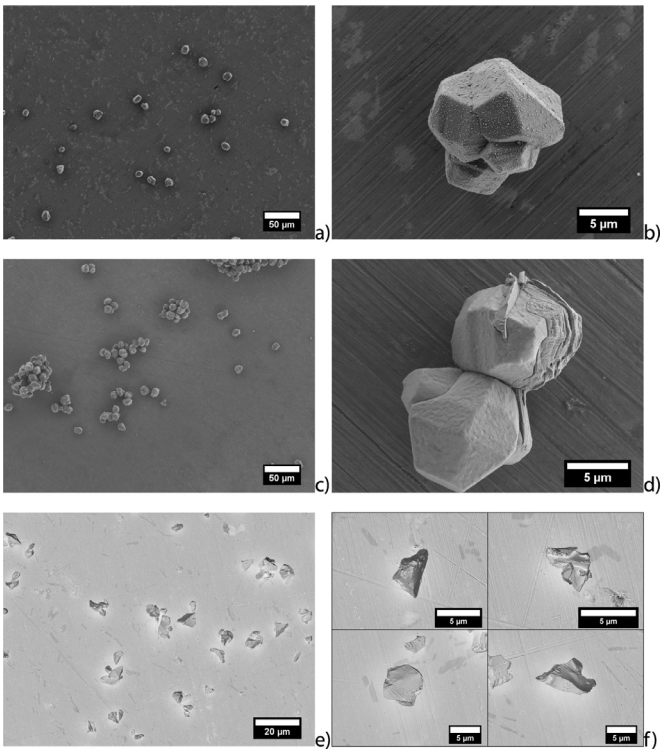

Fig. 1. SE-SEM images of the three powders used, (a) and (b) AA10, (c) and (d)β''-AA10 and (e) and (f) F1000.

To produce preforms for infiltration, alumina powders were compacted by cold isostatic pressing (CIP) at 150 MPa for 1 min. The produced CIPed preforms are cylinders approximately 14 mm in both diameter and height, Fig. 2. The ceramic reinforcement volume fraction (V_r) in the composite was measured by characterisation of the composites after full infiltration at 700°C, by densitometry using a Sartorius MC210P microbalance of sensitivity $\pm$ 10 μg. The measured V_r for F1000 is 0.52 (as in [18,25–27]). For β''-AA10 and AA10 V_r is 0.58. The average pore size as given by mercury porosimetry is 3.62 μm for the F1000 powder and 7.24 μm for both AA10 and β''-AA10 powders. For the metal matrix, 99.99% pure Al purchased from Hydro Aluminium GmbH (Germany) was used as the infiltrant in all experiments reported here.

2.2. Gas-pressure infiltration

Infiltration experiments comprising a dynamic measurement of the saturation were conducted for F1000, AA10 and β''-AA10 powder preforms infiltrated with molten aluminium at one of three temperatures, namely 1000°C, 1050°C or 1100°C. Each experiment was performed three times in order to test the reproducibility of the tests.

To have a reference state for the drainage curve of AA10 powders at the same temperatures but in the presence of much slower metal/ceramic interaction, one experiment was conducted in which Copper (Cu 99.99%) was infiltrated into a preform of AA10 powder at 1150°C.

All infiltration experiments other than at 1150°C were conducted using an instrumented infiltration apparatus, by means of which one can track with comparatively high precision the volume of metal that has penetrated the preform while pressure is applied to drive infiltration. This apparatus and basic features of the experiments are described in Refs. [18,26,28].

To explore the role played by sodium impurities in pressure infiltration, we performed an additional Al-F1000 infiltration at 1150°C

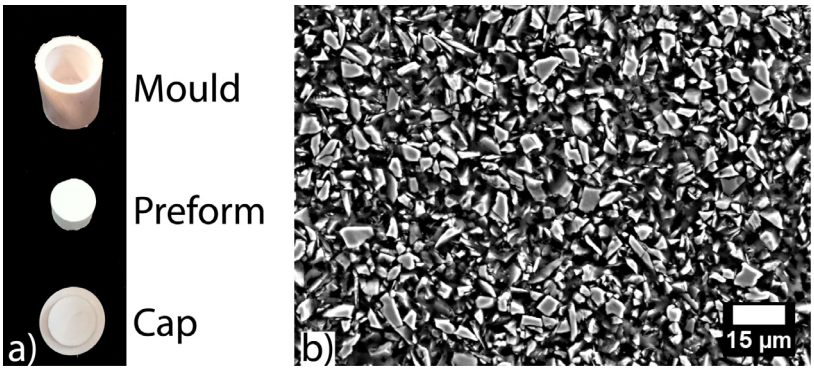

Fig. 2. (a) an as-ClPped (AA10) alumina powder preform 14 mm in diameter together with the rubber mould that was used to produce it; (b) scanning electron micrograph of an uninfiltrated portion of a F1000 preform (from an experiment conducted at 700°C), subsequently infiltrated with epoxy and polished, showing the close-packed powder making the preforms.

with the aim to characterize the composite microstructure after infiltration at that temperature and determine the nature of the oxide layer covering the melt after infiltration. The experiment consisted in producing a composite without tracking the fluid displacement (in order to have a clean liquid surface on the top of the sample), holding the system at 1150°C for 4 h under 4 MPa applied pressure to effect full infiltration and to give ample time for metal/ceramic chemical interaction.

In the present work, focused on the kinetics of infiltration in the presence of preform/infiltrant interaction, instead of measuring saturation curves as was done in Refs. [18,26,28], we measure isobaric infiltration *rates*, using the same approach as in Ref. [10]. In a nutshell, after initiating infiltration once the applied pressure exceeds a threshold value P_{th}, we measure steady infiltration velocities at two different pressures that differ only slightly, changing the pressure several times during infiltration, so as to separate the influence of pressure and saturation on infiltration velocity at each temperature. As in Ref. [10], those two pressures are respectively the infiltration threshold pressure P_{th} at which the metal is observed to first penetrate the preform, and a value only slightly higher than this, namely P_{th}+0.05 MPa.

In each infiltration experiment, once preform, metal, crucible and tracking system are assembled and placed within the apparatus, and the apparatus is securely closed, the system is first evacuated and then heated up to the desired temperature. The pressure is then increased until reaching the threshold pressure P_{th}, meaning until the tracking device records a displacement of the liquid front. Then, 0.05 MPa is added to the applied pressure. The pressure is thereafter held at that value until the melt penetration rate becomes constant over at least 120 s; more specifically, until $R^2 \geq 0.999$ over 120 s in a dynamic linear regression over points of melt height versus time recorded with a frequency of 10 Hz. It is important to note that such hold times and associated infiltration rates are such that the capillary number (velocity times viscosity divided by surface tension) falls far below unity, so that pressure drops across the liquid associated with viscous or inertial friction forces are negligible; see Ref. [26] for a further discussion of the matter.

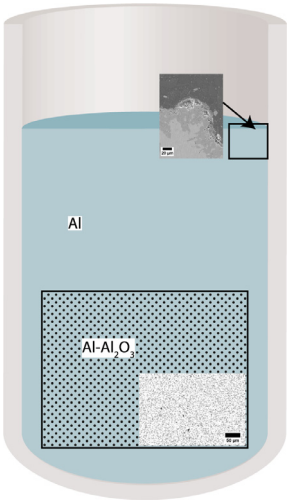

Fig. 3. Sketch of a cross section through the Al-F1000 sample produced at 1150°C for 4 h under a steady applied pressure of 4 MPa. Light blue is Al; the rectangular area represents the Al-Al_2O_3 composite (in the inset is an optical image of its microstructure). Along the top surface a rectangle and the inset micrograph represent the region where the oxide layer covering the Al melt was investigated (see discussion).

The data used to compute the saturation velocity ($\frac{dS}{dt}$) are saved with a frequency of 0.2 Hz. Once $\frac{dS}{dt}$ is recorded, the pressure is reduced by 0.05 MPa, from P_{th}+0.05 MPa to P_{th}, and the rate of steady infiltration over 120 s is measured following the same procedure and criterion. The pressure is then increased back to P_{th}+0.05 MPa, and this process is repeated between the two pressures (P_{th} and $P_{th} + 0.05$ MPa) until rates of infiltration are no longer measurable because steady infiltration rates decrease with increasing saturation. The pressure is then raised rapidly to 5 MPa in order to fully infiltrate the composite and to record the total displacement of the fluid, as this later allows to calculate the saturation corresponding to each recorded melt surface level.

This process, of shifting the applied pressure from P=P_{th} to P=P_{th}+0.05 MPa and back after the front has reached a sufficiently steady velocity, was repeated several times during each infiltration experiment, the number of pressure changes being mostly a function of the time taken by the infiltration front to stabilise to a sufficiently steady and measurable saturation increase rate. The end result of those measurements is the rate of steady increase in saturation $\frac{dS}{dt}$ for each system as a function of three main parameters, namely the applied pressure, the saturation and the temperature, together with measures of the effect of pressure alone since this parameter was shifted rapidly several times at fixed temperature over a narrow range of saturation values. In effect, present experiments are the infiltration-analogue of stress-jump tests in high-temperature plasticity.

2.3. Composite characterization

Microstructural characterization of the composite was conducted using standard metallographic procedures, in which a cross-section of the composites is embedded in a polymeric resin and polished down to $1\mu m$ diamond paste. The morphology of Al_2O_3 particles after infiltration was revealed by soaking a polished cross section of the composite in a solution of NaOH 1[M] for 60 s, followed by scanning

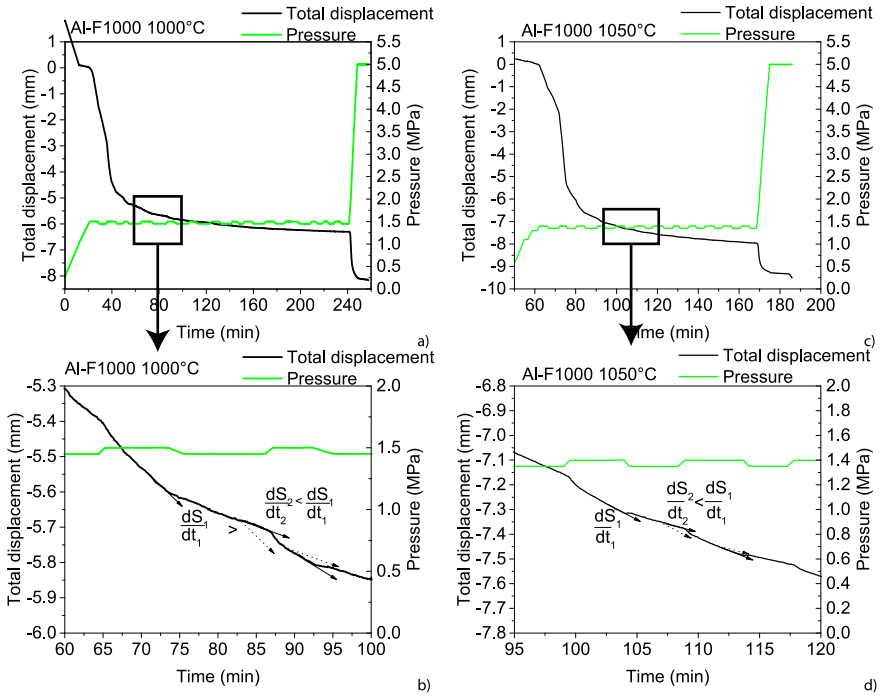

Fig. 4. Raw data for infiltration at 1000°C ((a) and (b)) and 1050°C ((c) and (d)) of the Al-F1000 system; (a) and (c): full infiltration displacement, (b) and (d): zoom showing the changes in velocity after a small pressure drop.

electron microscopic characterisation of particles that remained attached to the composite surface.

The phase composition of powders (in as-received condition or within infiltrated composites) was analysed by means of a Philips X-Pert X-Ray Diffractometer (XRD) equipped with a Cu-Kα source. Analyses were performed at 45 kV and 40 mA in a 5-90° 2θ range.

Microscopy was conducted using a Zeiss® Merlin SEM (Carl Zeiss, Germany) scanning electron microscope. Local elemental compositions were investigated by EDX (Energy Dispersive X-Ray) analysis using an Oxford Instrument apparatus mounted in the SEM with a voltage of 10 keV and a probe current of 700 pA. The software ETAS® INCA v.7.0 was used to quantify EDX results.

3. Results

3.1. Isobaric infiltration kinetics

3.1.1. Al-F1000 system

Two representative full infiltration curves of the Al-F1000 system at 1000°C are shown in Fig. 4(a) and (c). The last sudden increase in pressure was conducted at elevated saturation, once the measured saturation increase rates had become too small to be measured with precision, so as to effect full infiltration of the ceramic preform.

Fig. 4 (b) and (d) show close-ups over a portion of those curves. As seen, a change in the applied pressure causes a noticeable change in the saturation increase rate. This influence of the applied pressure on the infiltration rate was observed at all three temperatures of the present investigation. This differs from what was found at lower temperature in Ref. [18], where infiltration stabilized after some time, making possible at those temperatures the measurement of saturation curves, in which a single value of saturation characteristic of (static) capillary force equilibration is plotted for each value of the applied pressure.

Collating all infiltration velocity data for this system at 1000°C, 1050°C and 1100°C gives Fig. 5. As seen, $\frac{dS}{dt}$ shows a relatively high degree of variability, yet it transpires from the data that $\frac{dS}{dt}$ (i) increases with increasing P at given saturation and temperature, (ii) decreases with increasing saturation and (iii) does not vary systematically with increasing temperature: rates are in fact lowest at the highest temperature.

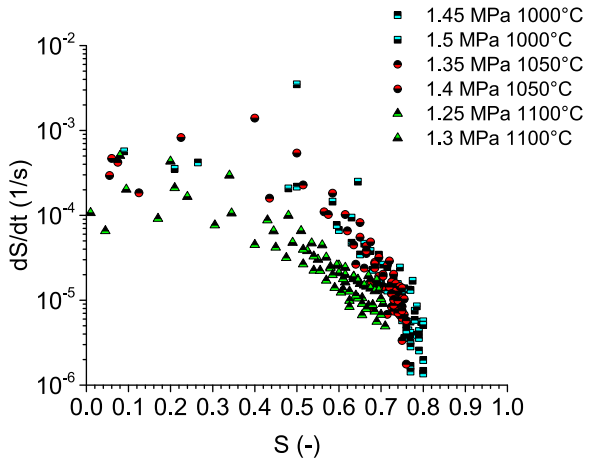

Fig. 5. Raw saturation velocities at three different temperatures for Al-F1000 composite infiltration; 1000°C (squares), 1050°C (circles) and 1100°C (triangles).

3.1.2. Al-AA10 system

Illustrative infiltration curves for Al-AA10 alumina at 1000°C and 1100°C, similar to those given for the F1000 powder, are given in Fig. 6(a-b) and Fig. 6(c-d), respectively. As seen, unlike what is observed with the F1000 powder, with AA10 powders the front stabilizes after each pressure change. The kinetic phenomenon responsible for the observation of sustained isobaric infiltration with the F1000 powder is thus either absent or much slower with the AA10 powder than it is with F1000 alumina.

Given that the front stabilizes with AA10, it is in principle possible to measure a drainage curve for this system. Such measurements were performed following the same procedure as was used for the Al-F1000 system in [18], where it was found that to obtain

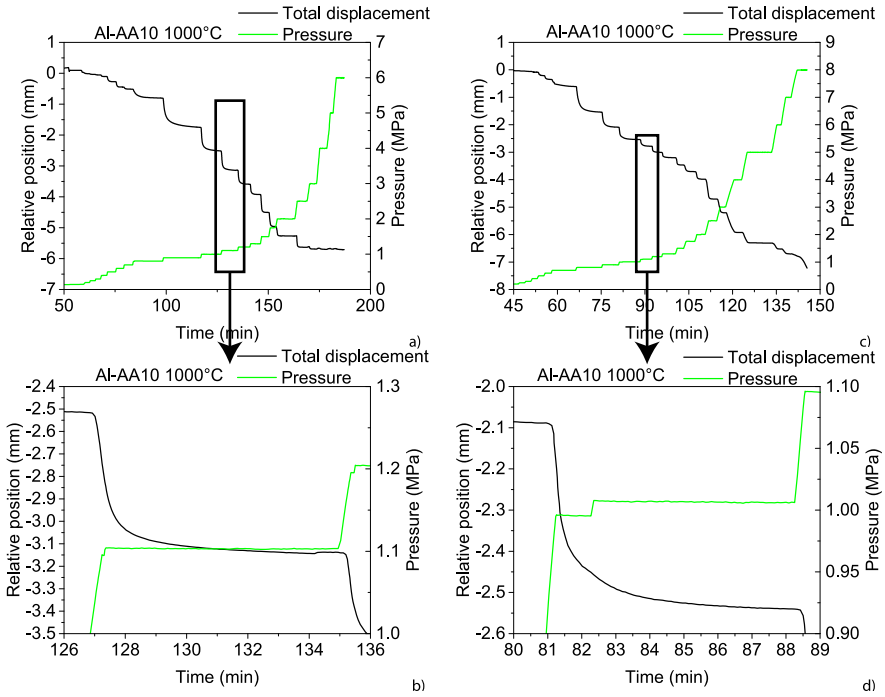

Fig. 6. Infiltration data for the Al-AA10 system at 1000°C. (a) and (c): full infiltration curve, (b) and (d): zoom at the end of the pressure step showing stabilization of the infiltration front.

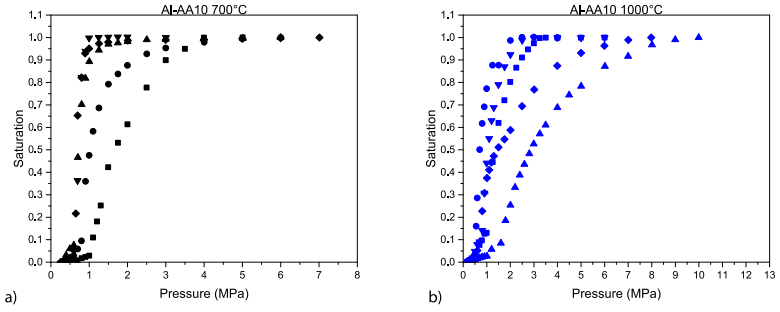

Fig. 7. Separately measured drainage curves for the system Al-AA10 showing the lack of reproducibility of the tests: infiltration at (a): 700°C, (b): 1000°C.

reproducible drainage curves with aluminium-containing melts at temperatures near the metal or alloy melting point, one had to first preheat the system to higher temperatures, of 1000°C or above, before infiltration at lower temperature. The system was thus preheated to 1000°C and then cooled down to 700°C before applying a sequence of increasing pressure values, recording the saturation reached after front stabilisation at each successively higher fixed infiltration pressure. Results of those measurements for the Al-AA10 system at 700°C and 1000°C are given in Fig. 7. As seen, the data are not reproducible: at both temperatures, a different drainage curve is obtained for each different experiment.

In summary, with the Al-AA10 system, (i) continued, steady, isobaric pressure infiltration is not observed and (ii) drainage curves are measurable, but are not reproducible. In both respects, thus, data differ from what is observed with F1000 alumina.

3.1.3. Al-β''-AA10 system

Repeating those experiments with the β''-AA10 powder, produced by incorporating sodium into the AA10 powder to the same concentration as in the F1000 powder, gives data exemplified at 1000°C in Fig. 8. As seen, as with the AA10 powder and unlike what is observed with the F1000 powder, the infiltration front stabilizes after a sufficiently long hold at fixed pressure ($\frac{dS}{dt} \approx 0$), Fig. 8(b).

Repeating hence with this powder drainage curve measurements that were conducted for the Al-F1000 system at lower temperature in Ref. [18] and here for the Al-AA10 system, gives results plotted in Fig. 9(a). As seen, with the β''-AA10 powder, there is sufficient reproducibility of Al infiltration at 1000°C to draw a meaningful drainage curve for this system.

For comparison purposes, we repeated these drainage curve measurements with the (non-reactive) Cu-AA10 system. To enable comparison with the Al-β''-AA10 system, results for both systems are combined in Fig. 9(b) after normalisation of the pressure by division with the work of immersion (surface tension σ_{LV} times $\cos(\theta)$). As seen, within experimental uncertainty, the curves superimpose. Figure 9(c) shows that the Brooks and Corey relation is obeyed, as has often been observed [18,25–37]. The exponent λ, known to be a characteristic of the pore (and hence particle) geometry, Fig. 9(c), is also a constant, as expected.

3.2. Phase characterization

Fig. 10 shows XRD spectra collected from Al-F1000 composites after full infiltration at 1000°C, 1050°C, 1100°C and 1150°C. For comparison, the XRD pattern collected from the pristine F1000 powder is reported in the same figure. As seen, after infiltration below 1150°C, the composites show the presence of Al, α-Al_2O_3 and a sodium-containing phase

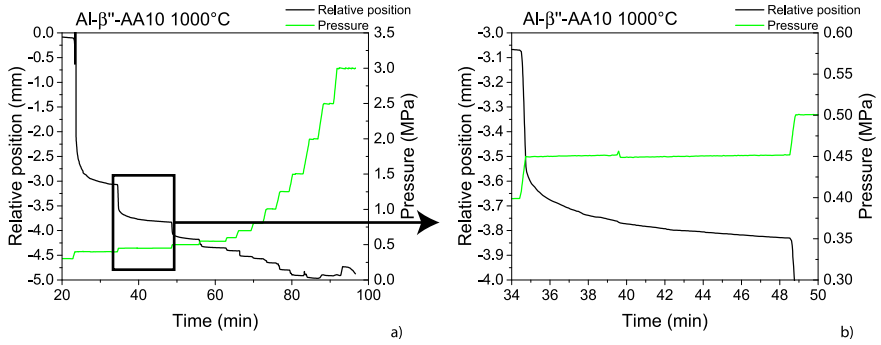

Fig. 8. Raw infiltration data for the system Al-β''-AA10 infiltrated at 1000°C (a) full curve, (b) zoom between two pressure steps showing that the front stabilizes when the pressure is held for a sufficiently long time.

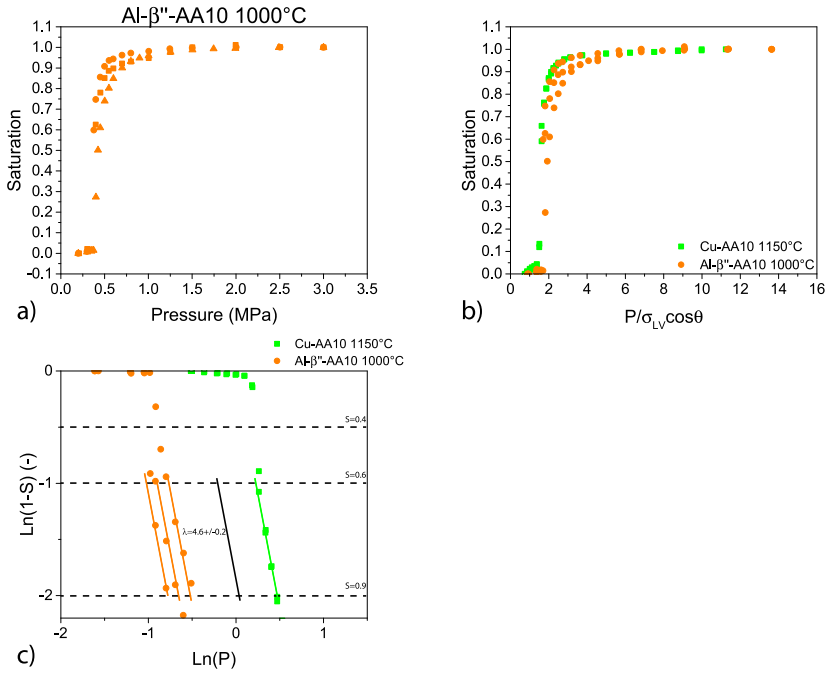

Fig. 9. (a) Drainage curves for the Al-β''-AA10 system at 1000°C, (b) comparison between the relative drainage curve of Al-β''-AA10 at 1000°C and Cu-AA10 at 1150°C and (c) Brooks and Corey relation for the two systems.

identified as $NaAl_{11}O_{17}$, also known as β'' alumina (note the low sodium content in the phase). The amount of (β''-Al_2O_3) phase relative to the amount of α-Al_2O_3 is lower after Al infiltration compared with the raw powder. The amount of β'' alumina decreases as the infiltration temperature increases, to reach zero in the composite produced by infiltrating F1000 powder with Al at 1150°C.

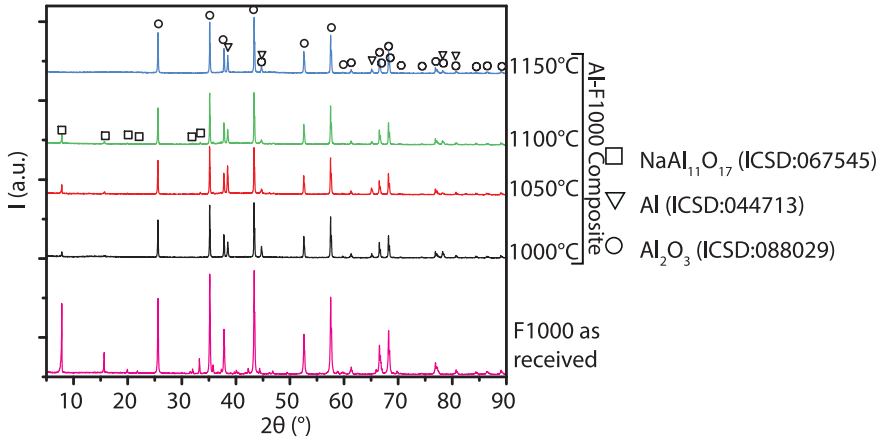

Fig. 10. XRD spectra of the as-received F1000 powder (bottom) and (from bottom to top) of the Al-F1000 composite infiltrated at 1000, 1050, 1100 and 1150°C.

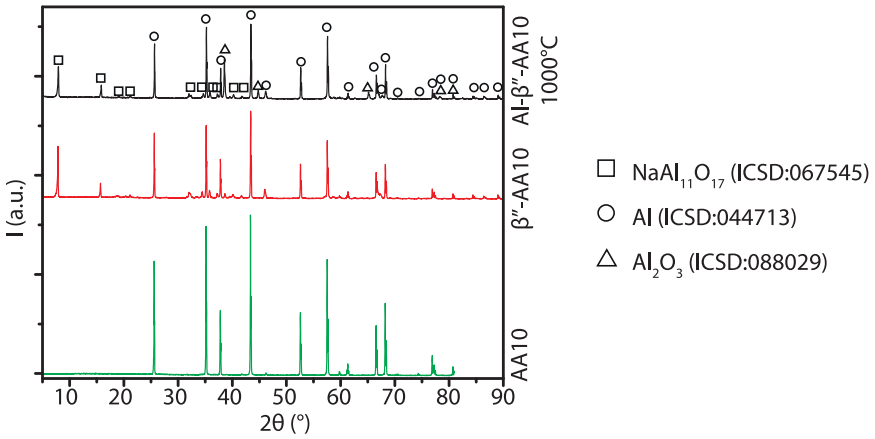

Fig. 11. XRD spectra of the Al-β''-AA10 composite infiltrated at 1000°C (black, top curve) compared to β''-AA10 (red) and AA10 (green, bottom curve) powders. (For interpretation of the references to color in this figure legend, the reader is referred to the web version of this article.)

Fig. 11 compares the XRD spectra of AA10 and β''-AA10 powders: this shows the presence of $NaAl_{11}O_{17}$ in the latter, in proportions similar to what is found in F1000. The Al-β''-AA10 composite infiltrated at 1000°C shows also the presence of this phase, albeit at a lower relative concentration compared to alpha-alumina than in the initial, as-reacted and uninfiltrated, β''-AA10 powder.

3.3. Composite microstructure

Fig. 12 shows back-scattered electron (BSE) images of the Al-F1000 composite infiltrated at 700°C (Fig. 12(a)) and at the three (higher) temperatures at which infiltration kinetics were measured (1000-1050-1100°C) (Fig. 12(b-d)). As seen, in the composite infiltrated at 700°C, F1000 particles retain their initial, highly irregular and angular, shape characteristic of comminuted powder (see Fig. 1 (e-f)), with sharp angles separating planes along which the material fractured in its production process. Fig. 12(b-d) show that, as the infiltration temperature increases, those sharp angles disappear. The particles have become increasingly rounded and show increasing levels of mutual coalescence.

The Al-AA10 composites (Fig. 13(a-d)) on the other hand do not show signs of such an evolution in their shape and size, regardless of the infiltration temperature. The etched sample (Fig. 13(c)) confirms that no change in powder morphology or size is visible after infiltration of those particles.

Finally, Fig. 14 show the microstructure of Al-β''-AA10 composites infiltrated at 1000°C. The microstructure is similar to that in Fig. 13, leading to conclude that adding sodium to AA10 does not alter the observation that there is no change in particle morphology or size after high-temperature infiltration with aluminium.

4. Discussion

4.1. Infiltration kinetics in the Al-Al_2O_3 system

Summing up, present data show that:

1. The triple line does not stabilize at, or above, 1000°C at fixed applied pressure during the pressure-infiltration of F1000 particle preforms with aluminium. An interfacial phenomenon drives the metal into the preform at fixed pressure, in the same way as does a wettability-enhancing interfacial reaction.
2. That this is observed neither with the Al-AA10 nor the Al-β''-AA10 systems implies that the interfacial phenomenon in question is not linked with the presence of sodium impurities in the F1000 powder.

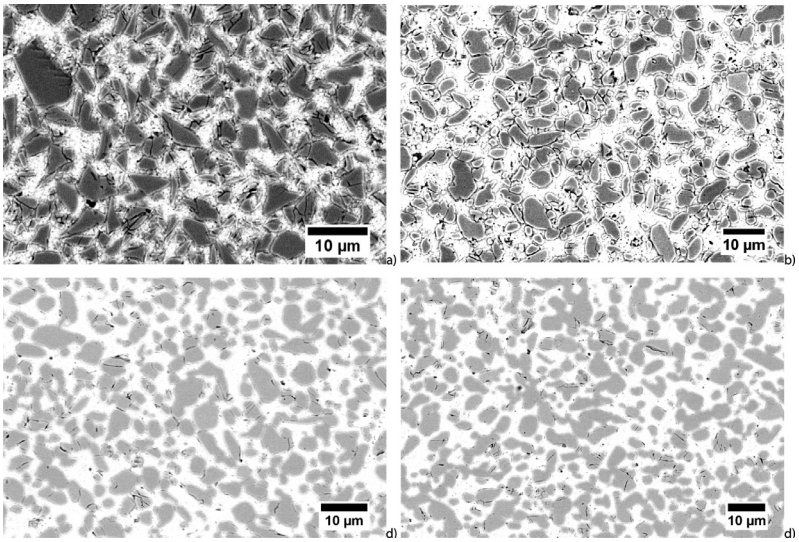

Fig. 12. Microstructure of the Al-F1000 composite infiltrated at (a) 700°C, (b) 1000°C, (c) 1050°C and (d) 1100°C.

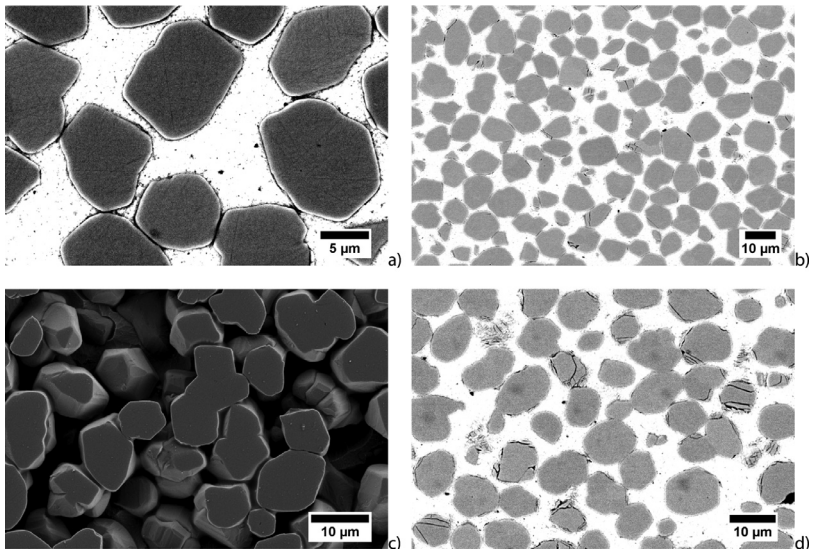

Fig. 13. Microstructure of the Al-AA10 composite infiltrated at (a): 700°C, (b) and (c): 1000°C; in (c) the surface is deep-etched in order to remove the matrix and highlight the shape of particles, and (d): Al-AA10 composite infiltrated at 1100°C.

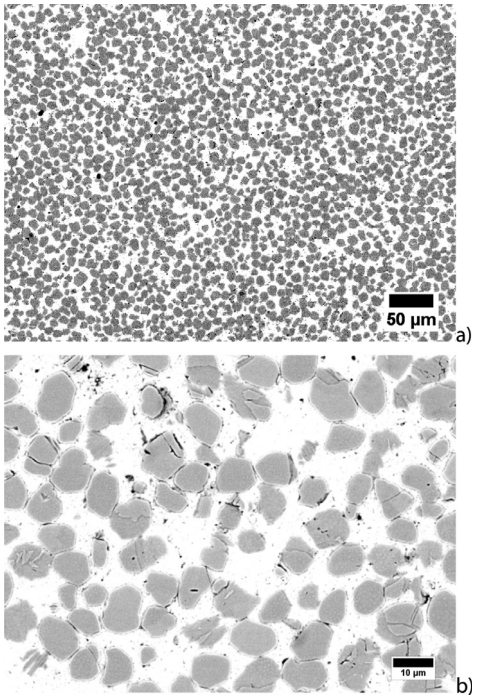

Fig. 14. Microstructure of the Al-β''-AA10 composite infiltrated at 1000°C (a) low magnification, (b) high magnification showing no modification of the particles after high temperature infiltration.

3. SEM images of Al-F1000 composites (Fig. 12) show that the particles have coarsened during infiltration at or above 1000°C, while after infiltration at 700°C the highly angular particle shape characteristic of communition is retained.

These three observations lead to conclude that the reason why one observes, at 1000°C or above, continuous isobaric infiltration in this system is that the liquid/solid interface becomes sufficiently mobile to enable the liquid metal meniscus to continuously advance forward under constant applied pressure. As such, this mechanism parallels the "ridging" process that was reported for sessile drop experiment data by Saiz, Tomsia *et al.* [5–9].

How such coarsening causes the continued forward motion of the infiltration front cannot be fully ascertained from the present data; however, a simple realistic scenario can be proposed. In preforms of the highly angular F-1000 particles, sharp angles along the surface of the particles provide pinning points along the path of forward motion of the liquid metal meniscus through the open pore space within the powder preform. Now, once the liquid metal contacts such pinning points, coarsening by solution-reprecipitation of alumina (likely either through the liquid metal or along the liquid/solid interface) will blunt solid ceramic ridges sharper than the value dictated by local triple line capillary equilibrium, leading to an opening of the passage letting the liquid metal meniscus to advance into the next pore. Such opening will lower the threshold pressure required for the metal surface to move past the pinning point, causing the meniscus to jump forward, despite the fact that the driving pressure is constant. A simple sketch of this process is presented in Fig. 15. Note also that, for a given reduction in the width of the narrowest constriction (and hence for a given decrease in the critical threshold pressure for passage of the meniscus), a greater volume of solid material must be displaced if the angle α characterizing the sharpness of the ridge along the surface of particles increases. The fact that ridges are more blunt (i.e., have wider initial ridge angles) and the particle size is larger in AA10 and β''-AA10 particles than in F1000 alumina can thus be advanced to explain why steady isobaric infiltration is not observed with those powders, while it is seen with the sharp and highly angular F1000 powder.

Having identified a plausible physical origin of steady infiltration with the Al-F1000 system, namely coarsening of sharp ridges along the alumina particles once these are in contact with molten aluminium, we seek to quantify features of this thermally activated isobaric infiltration process. We use the same approach (and make the same assumptions) as in Ref. [10], namely we link $\frac{dS}{dt}$ with the parameters of the thermally activated process through the relation:

$$\frac{dS}{dt} \propto \exp\left(\frac{-Q + V_a P}{k_B T}\right) \tag{2}$$

where $\frac{dS}{dt}$ is the saturation velocity, Q is the activation energy of the thermally activated phenomenon by which obstacles limiting motion of the liquid surface through the solid preform pore space are overcome, P the applied pressure, namely the pressure difference between the liquid and the initial atmosphere (vacuum usually), k_B is the Boltzmann constant and T is temperature. V_a is the relevant

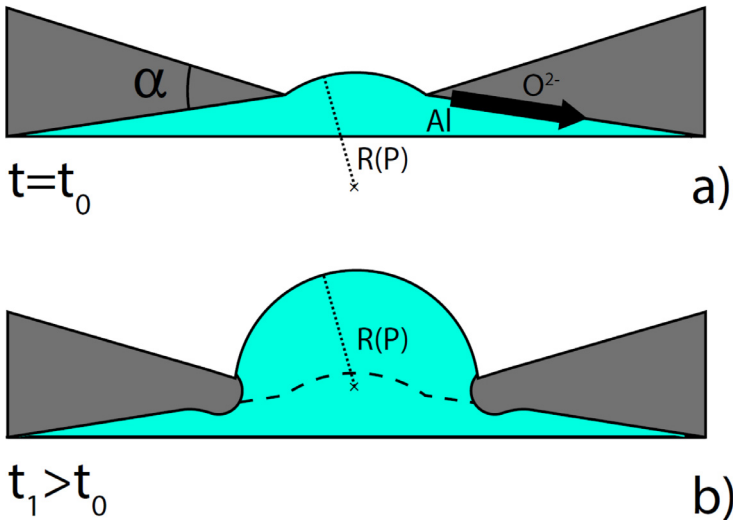

Fig. 15. Schematic showing a 2D liquid front making a finite equilibrium contact angle with the solid phase and reaching a pinning discontinuity presented by a (symmetric in this simple drawing) pair of particles having sharp ridges of angle α: (a) the applied pressure P is below the threshold for passage of the meniscus past the pinning point; (b) coarsening blunts the ridges and widens the passage, causing a gradual decrease in the critical threshold pressure and eventually releasing the meniscus.

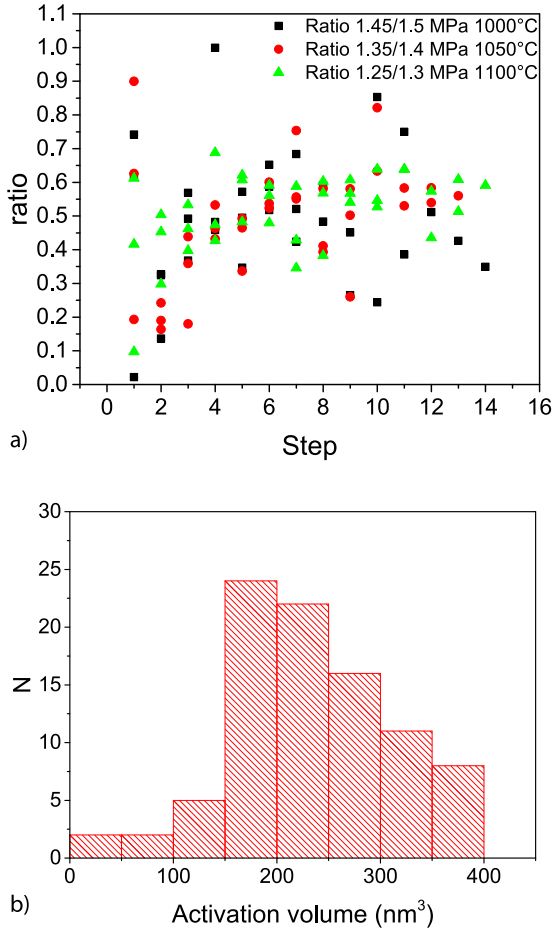

Fig. 16. (a) Ratio between measured rates of saturation increase across two successive stepped downward pressure changes across all experiments of this study, (b) histogram of the distribution of the corresponding activation volume values across all experiments.

activation volume; this represents, in addition to *Q*, a characteristic of the thermally activated process that drives gradual ingress of the liquid into pores within the solid under a finite applied pressure differential *P*.

V_a is deduced here by measuring infiltration rates at two different pressures, by writing as in Ref [10]:

$$\left.\begin{aligned}\frac{dS_1}{dt} &\propto \cdot \exp\left(\frac{-Q+V_aP_1}{k_BT}\right)\\ \frac{dS_2}{dt} &\propto \cdot \exp\left(\frac{-Q+V_aP_2}{k_BT}\right)\end{aligned}\right\} \begin{aligned}\ln\left(\frac{dS_1}{dt}\right) &= A+\frac{-Q}{k_BT}+\frac{V_aP_1}{k_BT}\\ \ln\left(\frac{dS_2}{dt}\right) &= A+\frac{-Q}{k_BT}+\frac{V_aP_2}{k_BT}\end{aligned}$$

$$\ln\left(\frac{dS_1}{dt}\right)-\ln\left(\frac{dS_2}{dt}\right)=\frac{V_a(P_2-P_1)}{k_BT}\Rightarrow V_a=-\ln\left(\frac{dS_1/dt}{dS_2/dt}\right)\cdot\frac{k_BT}{\Delta P} \quad (3)$$

where $\Delta P = P_2 - P_1$ and $\frac{(dS_i)}{dt}$ is the measured velocity at pressure P_i.

Using data giving the change in rate of saturation increase as one changes suddenly the infiltration pressure, we estimate the corresponding activation volume using the approach in Ref. [10]. The ratio of infiltration velocities for each successive downward change in the infiltration pressure is given in Fig. 16(a) for the three investigated temperatures (1000-1050-1100°C). As seen, there is considerable scatter in the data. This is particularly pronounced at low saturation, most likely because in early, low-saturation, phases of infiltration, measured infiltration velocities are more strongly influenced by percolation effects. These will introduce a higher level of stochasticity in infiltration data, causing more scatter in the rate of infiltration from one experiment to another, or as the saturation varies within a given infiltration experiment.

From the histogram in Fig. 16, one can deduce an estimated value of the activation volume for the pressure infiltration of Al into angular preforms of Al_2O_3 that is between 200 and 300 nm^3 (the computed average value is 235 nm^3 with a standard deviation of 80 nm^3). It is interesting to note that this value is not very different from what was recorded with the (chemically very different) Cu-Si/Carbon system, where it was found that $V_a \approx 200$ nm^3 Ref. [10]. That these two values be so close, despite the large differences between the two systems, suggests that the value of V_a may be related to the size of the "bulge" that must form along the solid/liquid/vapour triple line for a meniscus to break free, with help from the applied pressure, of a pinning point in either of the two systems.

If we now use $V_a = 235$ nm^3 in Eq. (2) to correct the saturation velocities for the influence of the applied pressure, then recorded saturation increase rates in Fig. 5 become pressure-compensated saturation increase rates plotted in Fig. 17. As seen, pressure-compensated infiltration rates are (contrary to the raw data) such that the higher

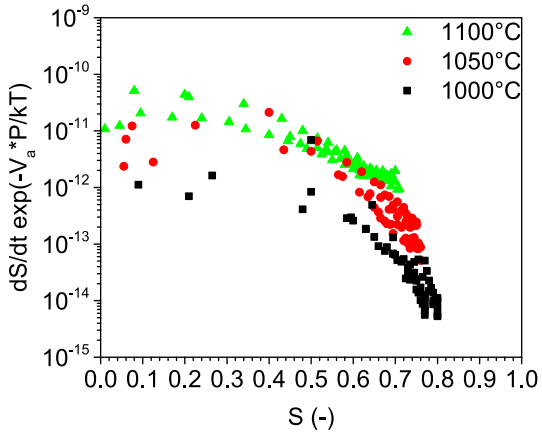

Fig. 17. Saturation velocities corrected for the influence of pressure and temperature using Eq. 2 and the average computed activation volume across all experiments of this study V_a=235 nm^3.

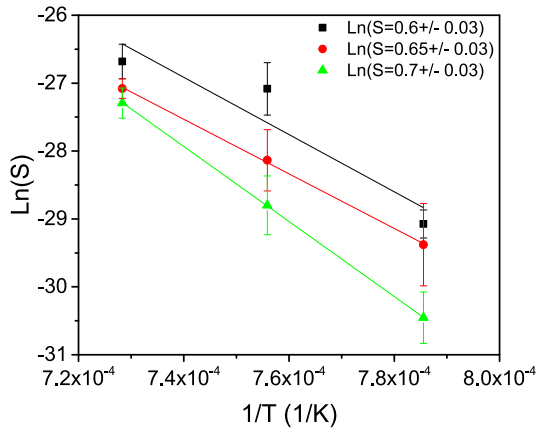

Fig. 18. Arrhenius plots for pressure-compensated infiltration rate data over the three infiltration temperatures around three values of saturation namely S = 0.6 ± 0.03, 0.65 ± 0.03 or 0.7 ± 0.03.

the temperature is, the faster the front moves, which is now as expected for a thermally activated phenomenon.

Having the pressure-compensated saturation velocities at different temperatures, one may seek to draw an Arrhenius plot to estimate the activation energy characteristic of the process driving steady pressure infiltration at high temperatures in this system. This is done in Fig. 18 using pressure-compensated saturation increase rates averaged over all data points in the range of saturation values within $\pm 0.03S$ of S= 0.6, 0.65 or 0.7. As seen, the degree of scatter in the average slopes through data points is higher than was found for Cu-Si alloy infiltration into carbon preforms; however, using the slope given by linear regression through each of the three sets of three temperatures explored one obtains calculated activation energies in Fig. 19. These vary from roughly 330 to 460 $\frac{kJ}{mol}$. Those are high values, consistent with the fact that at lower temperatures particle rounding or coarsening and gradual thermally activated isobaric infiltration are not observed. $Q \approx 400 \frac{kJ}{mol}$ is only somewhat lower than the activation energy for the diffusion of oxygen in alumina, reported to be between 450 $\frac{kJ}{mol}$ [38,39] and 600 $\frac{kJ}{mol}$ [40–44].

4.2. Effect of sodium impurities in alumina preforms on pressure infiltration with aluminium

Whereas sodium impurities in the alumina preform play no apparent role in the gradual, thermally activated, isobaric infiltration of F1000 preforms, our data show that they influence the

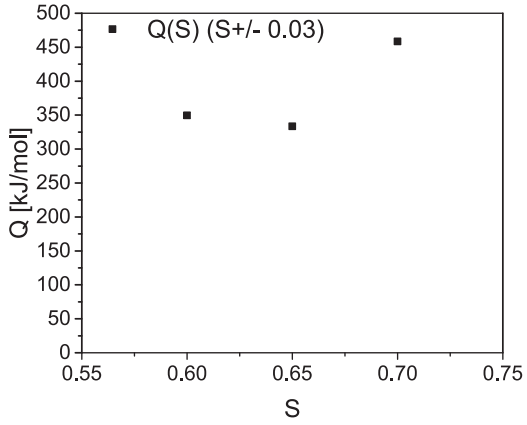

Fig. 19. Activation energy computed around three values of saturation namely S = 0.6 ± 0.03, 0.65 ± 0.03 or 0.7 ± 0.03.

reproducibility of drainage curve measurements in the Al-Al_2O_3 system. Specifically, comparing the behaviour of the two Al-AA10 and Al-β''-AA10 systems, one observes that, without sodium in the alumina powder, drainage curves are (i) erratic and (ii) fall to the right of the reproducible drainage curve obtained both with the sodium-contaminated powder or (after normalisation of pressures) with molten copper, see Figs. 6-8. Without sodium, measured drainage curves become erratic and correspond to higher pressures. This suggests that "something" hinders penetration of the molten aluminium into the preform if there are no sodium atoms in the alumina powder.

The same erratic behaviour, hindering the measurement of reproducible drainage curves with aluminium-containing melts in the infiltration of Al_2O_3 preforms, was already noticed by Léger *et al.* in their work on the infiltration of F1000 Al_2O_3 powder preforms at lower temperature than this work [18]. Specifically, they found that, by pre-heating the system to 1000°C before infiltration at a lower temperature (nearer 700°C), the measurement of drainage curves with aluminium-containing melts at those lower temperatures became reproducible. Without such a preheat, erratic results similar to those gathered here with the AA10 powder were obtained.

Pooling the present data together with those of Ref. [18] leads us to propose the following scenario to explain the role of sodium impurities in the infiltration of alumina preforms with aluminium-containing melts:

At elevated temperatures (significantly above 700°C), sodium within the particles reacts with the aluminium-containing melt. This

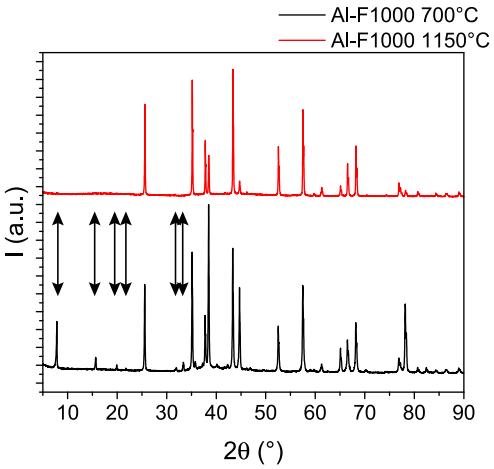

Fig. 20. XRD spectra for the composite infiltrated at 700°C (black, bottom) compared to the composite infiltrated at 1150°C (red, top). The arrows mark the main sodium phase peaks, which are not present in the latter composite.

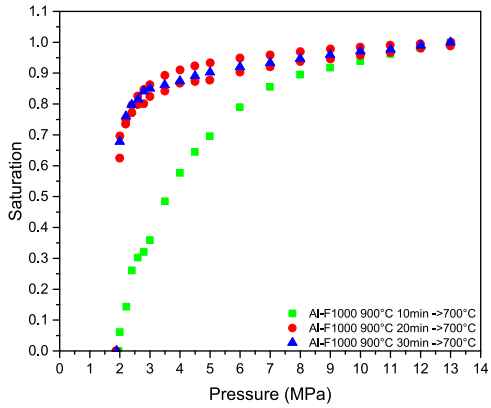

Fig. 21. Drainage curves for the Al-F1000 system measured at 700°C after pre-heating the system at 900°C for three different holding time values: 10 min, 20 min and 30 min respectively.

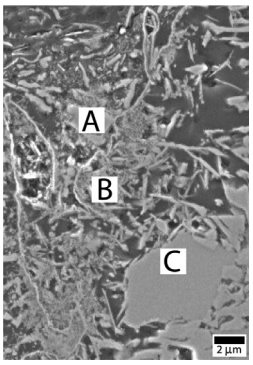

Fig. 22. Cross section of the liquid front along the top surface of an aluminium ingot used to infiltrate a F1000 preform at 1150°C for 4 h at 4 MPa. The locations of the EDX point analyses are labelled: at A and B one finds the sodium aluminate phase and at C the oxide layer is of pure alumina.

is shown by the decreased proportion of sodium-containing phase in the powders after infiltration at elevated temperature, see Figs. 10 and 11. Note that this leads to no modification of the composite microstructure, other than the gradual replacement of β'' alumina with α alumina within the particles. Sodium is not either to be found in the matrix nor along the interface of the particles if the composite microstructure is examined in the electron microscope. In summary, sodium is absent from the composite once it has left the ceramic powder.

It is interesting to note that, whatever interaction occurs between the melt and the powder, this interaction influences the course of infiltration *before* infiltration has started. This is evidenced by the fact that preheating the melt and (sodium-containing) alumina preforms to a temperature near 1000°C, before infiltration is conducted at a lower temperature, renders the drainage process reproducible at the lower temperature. Without such preheating, infiltration is erratic - and somehow hindered given that higher (and poorly reproducible) pressures are required to reach a given saturation.

To show that a thermally activated process occurs during the pre-heating step, we performed Al-F1000 infiltrations at 700°C after having pre-heated the system in vacuum to 900°C for respectively 10, 20 or 30 min. The corresponding drainage curves measured at 700°C are reported in Fig. 21. One sees that after holding the system for 20 min or more at T = 900°C, one starts to obtain reproducible results.

The most likely cause for the observed behaviour, which is not seen with melts that do not contain aluminium, is that the oxide layer that covers the surface of aluminium-containing melts is sufficiently thick and strong to hinder penetration of the preform unless it is altered; that this is so has been suggested by many authors before us (e.g., [17,30,45,46]). Léger *et al.* [18] proposed that the reason why preheating aluminium-containing melts to 1000°C before infiltration makes drainage curves reproducible could be that the aluminium oxide film on the liquid surface transforms itself into a gaseous aluminium oxide following the reaction:

$$Al_2O_3 \overset{\text{Heat}}{\rightarrow} Al_2O + O_2 \tag{4}$$

Present results show that this explanation cannot hold, since without sodium present, even when infiltration is performed at 1000°C, one does not obtain reproducible results with high-purity AA10 alumina preforms.

So why do small proportions of sodium in alumina aid infiltration with aluminium-containing melts if the melt and preform are pre-heated to sufficiently high temperatures for a sufficient time? Pooling data, we propose that this is because sodium is transported from the particles to the oxide that covers aluminium-containing melts, and alters it. Elrefaie and Smeltzer [23] show indeed that the $NaAl_{11}O_{17}$ phase has a partial pressure $p(Na) = 1 \cdot 10^{-7}$ at 1000°C and that if heated under vacuum it decomposes to form $Na_2O_{(v)}$+Al_2O_3. So it is plausible that at least some Na-O migrates away from the particles and reacts with the oxide layer that covers the liquid Al melt. Reported sodium aluminate densities are around 1.1 $\frac{g}{cm^3}$ [47]. This phase having a lower density than Al, it can float to the surface of the liquid metal, leaving the infiltration region and thus removing or altering the oxide layer that initially covers the metal. As a result, the mechanical hindrance that the oxide creates to penetration of the melt into open pores of the ceramic powder preform is reduced or removed.

To produce evidence of this, we performed an infiltration experiment free of melt tracking at 1150°C for 4 h at 4 MPa. The sample was heated under vacuum and then the chamber was pressurised to 4 MPa in order to fully infiltrate the composite. In the particles of this composite, no $NaAl_{11}O_{17}$ phase remains; this is evidenced by XRD data (Figs. 10 and 20). We examined the structure and composition of the oxide layer covering the melt along the top surface using optical and SE microscopy. To this end, the top of the Al ingot was cut after infiltration and solidification along its length and its cross section was analysed by SEM-EDX. A schematic representation of this sample showing the investigated zone is given in Fig. 3.

Fig. 22 shows the structure of oxide covering the metal along the top of the Al ingot: one finds alumina particles $> 10\ \mu m$ in size (C) together with needle- and platelet-shaped submicrometer particles (A and B) surrounded with Al metal. EDX analyses on those particles reveal the presence of Na, Al and O in the needle and platelet particles (A and B). This is consistent with the literature, which states that sodium aluminate phases often crystallise in platelet- or needle-like shapes [48]. More specifically, within error of EDX analyses, an average Na content of 1.5at.pct. was found, suggesting that this phase is $NaAl_{26}O_{40}$ (see Table 1) (~ Na_2O:Al_2O_3 1:26).

That Na is present on the top part of the Al ingot, and not inside the infiltrated composites, gives some credence to our proposal that Na impurities within alumina release sodium before infiltration, and that this sodium then interacts with the aluminium oxide film along the L-V interface in ways that make it less resistant or remove it, as does a flux, thus easing penetration of the melt into pores of the preform. This, in turn (i) makes drainage curve measurement reproducible and (ii) gives rise to a sodium aluminate phase that migrates to

Table 1
Summary of EDX analysis results of Fig. 22 in atomic percent.

Spot	O	Al	Na
A	64.6	32.9	2.6
B	60.1	38.4	1.5
C	66.9	33.1	0

the surface of the ingot, given that it is less dense than Al. The observation that the drainage curves of copper into AA10 and aluminium into β''-AA10 superimpose after division of the applied pressure by the relevant wetting parameters obtained from the sessile drop experiment in either of the two systems, Fig. 9, suggests that, once the oxide layer is cleaned off molten aluminium, one obtains results unperturbed by oxygen.

5. Conclusions

We show that:

- At 1000°C and above, the pressure infiltration of aluminium into Al_2O_3 particle preforms becomes time-dependent, showing steady penetration of the melt into the porous preform under fixed metal pressure if the alumina particles are highly angular. This feature, which can also be observed in reactive infiltration, is attributed here to solution-reprecipitation of the alumina in contact with aluminium, a process that bears strong similarity with the "ridging" mechanism that has been documented for this system in sessile drop wetting experiments. Interpreting the data using the same framework of analysis as that developed for elevated temperature dislocational plasticity leads to deduce that the thermally activated process underlying this gradual infiltration process is characterized by an activation volume on the order of $200nm^3$ and an activation energy in the range going roughly from 300 to $500\frac{kJ}{mol}$, a range near what has been measured for bulk diffusion of oxygen through alumina.
- The presence of sodium impurities in alumina, which react with an aluminium melt at 900°C and above, eases the initiation of infiltration, rendering the measurement of drainage curves reproducible. Present data give strong evidence that this is due to a fluxing effect exerted by sodium, which migrates at those temperatures out of the preform and likely interacts with the oxide layer that initially covers the aluminium melt, eliminating it by flotation or reducing its mechanical strength, such that it no longer opposes penetration of the melt into the powder preform.

Declaration of Competing Interest

The authors declare that they have no known competing financial interests or personal relationships that could have appeared to influence the work reported in this paper.

Acknowledgement

This work was sponsored by the Swiss National Foundation (FNS), Project No. 200021_ 149899. The authors are grateful to Professor F. Stellacci, of EPFL, Professor W. C. Carter, of MIT, and Professor J.-M. Molina-Jorda, of the University of Alicante, for enlightening discussions and helpful suggestions through this study.

References

[1] N. Eustathopoulos, D. Chatain, L. Coudurier, Wetting and interfacial chemistry in liquid metal-ceramic systems, Mater. Sci. Eng. A 135 (C) (1991) 83–88, doi: 10.1016/0921-5093(91)90541-T.
[2] E. Louis, J. Narciso, Pressure infiltration of packed ceramic particulates by liquid metals, Acta Mater. 47 (Section 4) (1999) 4461–4479.
[3] N. Eustathopoulos, B. Drevet, Interfacial bonding, wettability and reactivity in metal/oxide systems, J. Phys. III 4 (10) (1994) 1865–1881, doi: 10.1051/jp3:1994244.
[4] N. Eustathopoulos, R. Voytovych, The role of reactivity in wetting by liquid metals: a review, J. Mater. Sci. 51 (2016) 425–437, doi: 10.1007/s10853-015-9331-3.
[5] E. Saiz, R.M. Cannon, A.P. Tomsia, Energetic and atomic transport at liquid metal/Al_2O_3 interfaces, Acta Mater. 41 (15) (1999) 4209–4220.
[6] E. Saiz, A.P. Tomsia, R.M. Cannon, Ridging effects on wetting and spreading of liquids on solids, Acta Mater. 46 (7) (1998) 2349–2361, doi: 10.1016/S1359-6454(98)80016-5.
[7] E. Saiz, A.P. Tomsia, Atomic dynamics and Marangoni films during liquid-metal spreading., Nat. Mater. 3 (December) (2004) 903–909, doi: 10.1038/nmat1252.
[8] E. Saiz, A.P. Tomsia, K. Suganuma, Wetting and strength issues at Al/α-alumina interfaces, J. Eur. Ceram. Soc. 23 (2003) 2787–2796, doi: 10.1016/S0955-2219(03)00290-5.
[9] G. Levi, W.D. Kaplan, Aluminium-alumina interface morphology and thermodynamics from dewetting experiments, Acta Mater. 51 (2003) 2793–2802, doi: 10.1016/S1359-6454(03)00084-3.
[10] G. Schneider, L. Weber, A. Mortensen, Reactive pressure infiltration of Cu-46% Si into carbon, Submitted to Acta Mater. (2019).
[11] J.A. Champion, B.J. Keene, J.M. Sillwood, Wetting of aluminium oxide by molten aluminium and other metals, J. Mater. Sci. 4 (1969) 39–49.
[12] M. Ksiazek, N. Sobczak, B. Mikulowski, W. Radziwill, I. Surowiak, Wetting and bonding strength in Al/Al_2O_3 system, Mater. Sci. Eng. A 324 (2002) 162–167.
[13] J.-M. Molina-Jordá, R. Voytovych, E. Louis, N. Eustathopoulos, The surface tension of liquid aluminium in high vacuum: the role of surface condition, Int. J. Adhes. Adhes. 27 (2007) 394–401, doi: 10.1016/j.ijadhadh.2006.09.006.
[14] V. Laurent, D. Chatain, C. Chatillon, N. Eustathopoulos, Wettability of monocrystaline alumina by aluminium between its melting point and 1273K, Acta Metall. 36 (7) (1988) 1797–1803.
[15] S. Bao, K. Tang, A. Kvithyld, T.A. Engh, M. Tangstad, Wetting of pure aluminium on graphite, SiC and Al_2O_3 in aluminium filtration, Trans. Nonferrous Metals Soc. China 22 (2012) 1930–1938, doi: 10.1016/S1003-6326(11)61410-6.
[16] A. Sangghaleh, M. Halali, Effect of magnesium addition on the wetting of alumina by aluminium, Appl. Surf. Sci. 255 (2009) 8202–8206, doi: 10.1016/j.apsusc.2009.05.044.
[17] S. Bao, K. Tang, A. Kvithyld, M. Tangstad, T.A. Engh, Wettability of aluminum on alumina, Metall. Mater. Trans. A 42B (2011) 1358–1366, doi: 10.1007/s11663-011-9544-z.
[18] A. Léger, L. Weber, A. Mortensen, Influence of the wetting angle on capillary forces in pressure infiltration, Acta Mater. 91 (2015) 57–69, doi: 10.1016/j.actamat.2015.03.002.
[19] A.R. Hind, S.K. Bhargava, S.C. Grocott, The surface chemistry of Bayer process solids: a review, Colloids Surf. 146 (1999) 359–374.
[20] R. Stevens, J.G.P. Binner, Review Structure, properties and production of β-alumina, J. Mater. Sci. 19 (1984) 698–715.
[21] G. Yamaguchi, K. Suzuki, On the structures of alkali polyaluminates, Bull. Chem. Soc. Jpn. 41 (1968) 93–99.
[22] R.C. De Vries, W.L. Roth, Critical evaluation of the literature data on beta alumina and related phases: I, Phase equilibria and characterization of beta alumina phases, J. Am. Ceram. Soc. 52 (7) (1969) 364–369, doi: 10.1111/j.1151-2916.1969.tb11956.x.
[23] F.A. Elrefaie, W.W. Smeltzer, Thermodynamic properties of the ionic conduction phases of Na-Al-O system between 800 and 1200 K, Solid State Ionics 12 (1984) 517–524.
[24] T. Takahashi, K. Kuwabara, β-Al_2O_3 synthesis from m-Al_2O_3, J. Appl. Electrochem. 10 (1980) 291–297.
[25] A. Léger, L. Weber, A. Mortensen, Infiltration of tin bronze into alumina particle beds: influence of alloy chemistry on drainage curves, J. Mater. Sci. 49 (2014) 7669–7678, doi: 10.1007/s10853-014-8475-x.
[26] A. Léger, N. Rojo-Calderon, R. Charvet, W. Dufour, C. Bacciarini, L. Weber, A. Mortensen, Capillarity in pressure infiltration: improvements in characterization of high-temperature systems, J. Mater. Sci. 47 (24) (2012) 8419–8430, doi: 10.1007/s10853-012-6645-2.
[27] A. Léger, J.-M. Molina-Jordá, L. Weber, A. Mortensen, Percolation and universal scaling in composite infiltration processing, Mater. Res. Lett. 3 (1) (2015) 7–15, doi: 10.1080/21663831.2014.948692.
[28] M. Bahraini, J.-M. Molina-Jordá, M. Kida, L. Weber, J. Narciso, A. Mortensen, Measuring and tailoring capillary forces during liquid metal infiltration, Curr. Opin. Solid State Mater.Sci. 9 (4-5) (2005) 196–201, doi: 10.1016/j.cossms.2006.02.007.
[29] M. Bahraini, Characterization of Capillarity Forces During Liquid Metal Infiltration, EPFL, 2007 Ph.D. thesis.
[30] V. Michaud, L. Compton, A. Mortensen, Capillarity in isothermal infiltration of alumina fiber preforms with aluminum, Metall. Mater. Trans. A 25 (10) (1994) 2145–2152, doi: 10.1007/BF02652315.
[31] V. Michaud, A. Mortensen, Infiltration processing of fibre reinforced composites: governing phenomena, Compos. Part A 32 (2001) 981–996.
[32] M. Bahraini, L. Weber, J. Narciso, A. Mortensen, Wetting in infiltration of alumina particle preforms with molten copper, J. Mater. Sci. 40 (9-10) (2005) 2487–2491, doi: 10.1007/s10853-005-1980-1.
[33] T. Dopler, A. Modaressi, V. Michaud, Simulation of metal-matrix composite isothermal infiltration processing, Metall. Mater. Trans. B 31B (2000) 225–234.
[34] M. Kida, M. Bahraini, J.-M. Molina-Jordá, L. Weber, A. Mortensen, High-temperature wettability of aluminum nitride during liquid metal infiltration, Mater. Sci. Eng. A 495 (1-2) (2008) 197–202, doi: 10.1016/j.msea.2007.12.050.
[35] V. Michaud, A. Mortensen, On measuring wettability in infiltration processing, Scr. Mater. 56 (10) (2007) 859–862, doi: 10.1016/j.scriptamat.2007.02.002.
[36] J.-M. Molina-Jordá, A. Rodríguez-Guerrero, M. Bahraini, L. Weber, J. Narciso, F. Rodríguez-Reinoso, E. Louis, A. Mortensen, Infiltration of graphite preforms with Al–Si eutectic alloy and mercury, Scr. Mater. 56 (11) (2007) 991–994, doi: 10.1016/J.SCRIPTAMAT.2007.01.042.

[37] H. Kaufmann, A. Mortensen, Wetting of SAFFIL alumina fiber preforms by aluminum at 973 K, Metall. Trans. A 23 (7) (1992) 2071–2073, doi: 10.1007/BF02647554.
[38] A.E. Paladino, W.D. Kingery, Aluminum ion diffusion in aluminum oxide, J. Chem. Phys. 37 (5) (1962) 957–962, doi: 10.1063/1.1733252.
[39] J.H. Harding, K.J.W. Atkinson, R.W. Grimes, Experiment and theory of diffusion in alumina, J. Am. Ceram. Soc. 86 (4) (2003), doi: 10.1111/j.1151-2916.2003.tb03340.x.554–59
[40] Y. Oishi, W.D. Kingery, Self-diffusion of oxygen in single crystal alumina, J. Chem. Phys. 33 (1960) 1679, doi: 10.1063/1.1731170.
[41] Y. Oishi, K. Ando, Y. Kubota, Self-diffusion of oxygen in single crystal and polycrystalline aluminum oxide, J. Chem. Phys. 73 (1980) 1410–1412, doi: 10.1063/1.440201.
[42] K.P.R. Reddy, A.R. Cooper, Oxygen diffusion in sapphire, J. Am. Ceram. Soc. 65 (12) (1982) 634–638, doi: 10.1111/j.1151-2916.1982.tb09944.x.
[43] D. Prot, M. Le Gall, B. Lesage, A.M. Huntz, C. Monty, Self-diffusion in α-Al_2O. IV. Oxygen grain-boundary self-diffusion in undoped and yttria-doped alumina polycrystals, Philos. Mag. A 73 (4) (1996) 935–949, doi: 10.1080/01418619608243697.
[44] D.J. Reed, B.J. Wuensch, Ion-probe measurement of oxygen self-diffusion in single-crystal Al_2O_3, J. Am. Ceram. Soc. 63 (1-2) (1980) 88–92, doi: 10.1111/j.1151-2916.1980.tb10655.x.
[45] A. Alonso, A. Pamies, J. Narciso, C. García-Cordovilla, E. Louis, Evaluation of the wettability of liquid aluminum with ceramic particulates (SiC, TiC, Al2O3) by means of pressure infiltration, Metall. Trans. A 24 (June) (1993) 1423–1432, doi: 10.1007/BF02668210.
[46] A. Demir, N. Altinkok, Effect of gas pressure infiltration on microstructure and bending strength of porous Al_2O_3/SiC-reinforced aluminium matrix composites, Compos. Sci. Technol. 64 (13-14) (2004) 2067–2074, doi: 10.1016/J.COMPSCITECH.2004.02.015.
[47] J.G. Reynolds, R. Carter, Density model for sodium hydroxide-sodium aluminate solutions, Hydrometallurgy 89 (2007) 233–241, doi: 10.1016/j.hydromet.2007.07.008.
[48] C. Zhu, J. Xue, G. Ji, Effect of Na_2O content on properties of beta alumina solid electrolytes, Mater. Sci. Semicond. Process. 31 (2015) 487–492, doi: 10.1016/j.mssp.2014.12.038.